Chemical Science

Accepted Manuscript

This article can be cited before page numbers have been issued, to do this please use: D. Rademaker, R. Maas, S. Tanase, H. Kang, J. P. Hofmann and D. Hetterscheid, *Chem. Sci.*, 2026, DOI: 10.1039/D6SC01428C.

ROYAL SOCIETY OF CHEMISTRY

rsc.li/chemical-science

View Article Online
DOI: 10.1039/D6SC01428C

ARTICLE

Instability of PCN-224(Fe) during the Oxygen Reduction Reaction; Metal-Organic Framework Electrocatalysts may have an Achilles heel

Received 00th January 20xx,
Accepted 00th January 20xx

DOI: 10.1039/x0xx00000x

Dana Rademaker,[a] Roy Maas,[a] Stefania Tanase,[b] Hongrui Kang,[c] Jan P. Hofmann[c] and Dennis G. H. Hetterscheid*[a]

Incorporation of catalytic sites within metal-organic frameworks has been considered advantageous as the amount of catalytic sites per cm^2 electrode surface and be greatly expanded, while simultaneously the stability of the catalytic sties can be greatly improved. In contrast to previous studies, it is found that the *d*PCN-224(Fe) catalyst is extremely sensitive towards reactive oxygen species (ROS) formation during the electrochemical oxygen reduction reaction and deactivates within seconds. Very little is known about deactivation of catalytic sites in MOFs and what the effect could be on the overall catalytic performance of the MOF as a function of time. Herein, the degradation mechanism of *d*PCN-224(Fe) with ROS is studied in detail and it is shown that a few catalytic sites – presumably positioned at the interface between the MOF and the carbon support – are the specific sites targeted by ROS leading to the complete breakdown of all activity. Therefore, even though the density of active sites is exceptionally high in MOF systems, the catalytic reaction is strongly dependent on only few active sites that are directly positioned at the connection between the MOF and the carbon electrode or support.

Introduction

Metal-organic frameworks (MOFs) are three-dimensional structures made from inorganic nodes and (metal-)organic linkers. Due to the tunability and the porous structure of MOFs, they have gained attention as electrocatalyst for small molecule conversions.[1-7] The porous structure allows for a large active surface area wherein well-defined catalytic sites are embedded at the node, linker, or as a guest directly at the working electrode of an electrochemical set-up.[8, 9]

Despite the potential of MOFs in catalysis thus far only a single application has made it to the market,[10] which is mostly due to an unfavourable ratio between synthetic costs[11] and MOF stability during catalytic performance. The stability of MOF-catalysts has predominantly been discussed in terms of the thermodynamics of linker – node interactions.[12-14] Particularly high valent metal sites, such as Zr^{IV} or Ti^{IV}, in combination with carboxylate functionalized linkers have been reported to be very robust.[15] However, the +IV oxidation state in case of titanium and zirconium is very favourable, making these sites unreactive in redox catalysis or electron shuttling.[9] Consequently additional redox sites and catalytic sites need to be implemented within such MOFs to mediate electrocatalysis.[16-18] Whereas confinement effects to facilitate the activation of reactants is often discussed to improve the activity and/or selectivity of catalytic sites within MOFs,[19, 20] confinement effects have rarely been discussed as a trigger for catalyst degradation. The local confinement of reagents, pollutants[21] and products may for example trigger significant local pH swings,[22] or accumulation of other reactive species. To understand how MOF breakdown during electrocatalysis occurs it is important to consider where the catalytic activity takes place during electrocatalysis in MOFs. Where catalysis occurs precisely depends on the diffusion of substrate to the active site, the charge transfer of electrons and ions through the framework, and the intrinsic catalytic rate at these specific active sites.[23-25] Depending on the limiting factor during catalysis, the number of active sites that participate in the catalytic reaction may therefore vary (Figure 1). When the diffusion of the substrate is rate limiting, it is expected that catalysis will predominantly occur at the catalytic sites at the borders of a MOF particle. When the catalytic reaction is limited by charge transfer it is expected that mostly catalytic sites near the interface of the electrode will react. When the catalytic reaction is limited by the intrinsic catalytic rate at an individual site, it is expected that the catalytic reaction will occur more homogeneously throughout the entire MOF particle. Which of these factors is limiting depends on the precise reaction conditions, which includes the concentration of ions, the concentration of substrate, and the applied potential. At the start of the electrolysis the catalytic reaction likely starts at the interface of the MOF crystal and its support, given that the reactant is already loaded within the MOF, and then sweeps through the crystal when the substrate concentration is locally

[a] Leiden Institute of Chemistry, Leiden University, 2300 RA Leiden, The Netherlands. E-mail: d.g.h.hetterscheid@chem.leidenuniv.nl.
[b] Van 't Hoff Institute for Molecular Sciences, Universiteit van Amsterdam, 1098 XH Amsterdam, The Netherlands.
[c] Surface Science Laboratory, Department of Materials- and Geosciences, Technical University of Darmstadt, Peter-Grünberg-Straße 4, 64287 Darmstadt, Germany.

depleted. At these sites where catalysis occurs also damage to the MOF-structure may be expected.

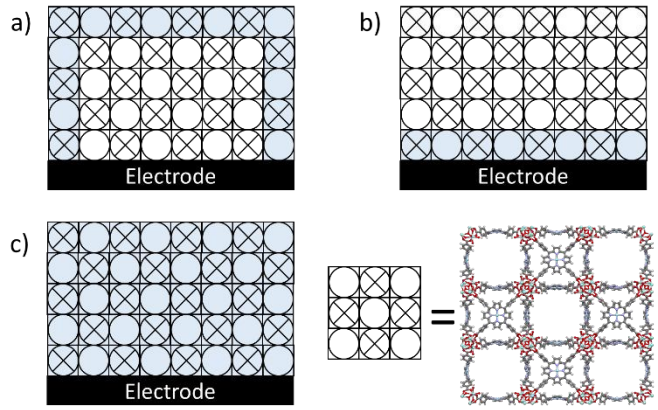

Figure 1. A cartoon of a PCN-224 MOF on an electrode with active sites participating in catalysis shaded in blue with the limiting factor of catalysis being (a) the diffusion of substrate, (b) the conduction of electrons and ions, and (c) the intrinsic catalytic activity of an individual active site. The crystallographic data was obtained from [26].

We recently reported PCN-224(Co) with the cobalt 5,10,15,20-(4-carboxyphenyl)-porphyrin chloride (CoTCPP) as linker as an effective catalyst for the oxygen reduction reaction (ORR) with a high selectivity toward H_2O_2 of 80%.[27] Moreover, the MOF was found to be highly stable upon build-up of H_2O_2 in the electrolyte solution. This high stability is an interesting finding as H_2O_2 is a strong oxidant that could lead to deactivation of catalytic sites if they were prone to oxidation by H_2O_2. The iron porphyrin-based MOFs PCN-224(Fe) and PCN-222(Fe) also showed to be active toward the electrochemical oxygen reduction reaction (ORR) under alkaline aqueous conditions and under acidic aqueous conditions, respectively.[28, 29] Iron 5,10,15,20-(4-carboxyphenyl)-porphyrin chloride (FeTCPP) is the active site in these porphyrin MOFs and during the ORR with this catalyst, the 2-electron ORR towards H_2O_2 formation is in competition with the 4-electron reduction towards H_2O (Figure 2).[30-32] The H_2O_2 formed at the iron porphyrin sites can be activated via the Fenton reaction to form reactive oxygen species (ROS).[33-40]

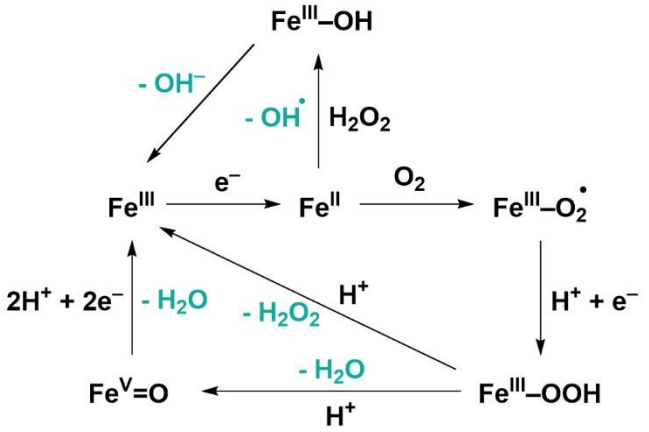

Figure 2. Mechanism of the ORR and Fenton reaction with iron porphyrin catalysts.[30, 31]

Here it is found that the catalytic sites in the dPCN-224(Fe) catalyst are extremely sensitive under ORR conditions and deactivate within seconds. With the hypothesis in mind that MOF degradation pathways may be MOF specific due to the confinement of reactants, and local due to the catalytic reaction within the MOF not occurring uniformly (illustrated in Figure 1) we studied the degradation mechanism of PCN-224(Fe) in the presence of O_2 in detail. It is for the first time reported that a few catalytic sites that are presumably positioned at the interface between the MOF and the carbon support are the specific sites that are presumably targeted by ROS leading to the complete breakdown of all ORR activity.

Results

PCN-224(Fe) was synthesized via a solvothermal synthesis by combining $ZrCl_4$ and FeTCPP with benzoic acid as modulator in dimethylformamide as solvent.[41, 42] The framework that was formed was characterized by scanning electron microscopy (SEM), powder X-ray diffraction (pXRD), and N_2-isotherm measurements. SEM images were collected from a drop of PCN-224(Fe) ink suspension, which contained PCN-224(Fe), carbon black, Nafion and acetone. The SEM images indicate a cubic morphology of the particles in the range of 1-4 µm, which agrees with the reported structure of PCN-224 (Figure 3).[43]

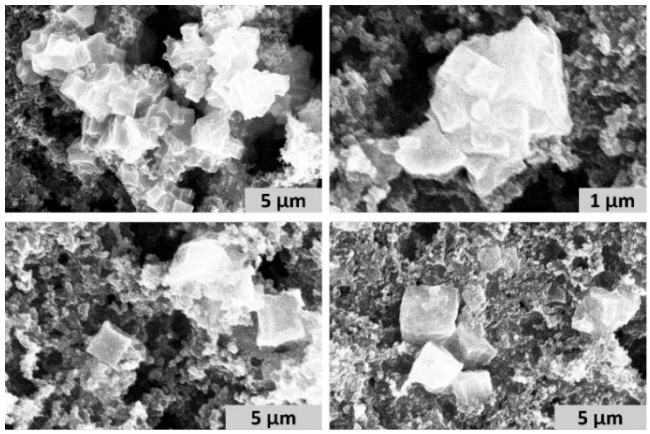

Figure 3. SEM image of PCN-224(Fe) ink measured at 15 kV and 0.1 nA.

The X-ray powder diffractogram matches the theoretical diffractogram of PCN-224, but lacks the reflections at 3.2 and 5.5° that indicate the presence of ordered PCN-224 superstructure domains in the MOF (Figure 4).[44] Therefore, the PCN-224(Fe) sample made in this work shows the reflections of a crystalline, but disorganized *d*PCN-224 structure.[43, 44] The MOF sample is therefore named *d*PCN-224(Fe). Furthermore, analysis of the N_2-isotherm indicated pore sizes of 0.8 and 2.0-2.5 Å, as expected for PCN-224 (Figure S1).[26] Combined, these analytical data for the MOF sample are in good agreement with a *d*PCN-224 sample of good crystallinity.[43]

View Article Online
DOI: 10.1039/D6SC04108C

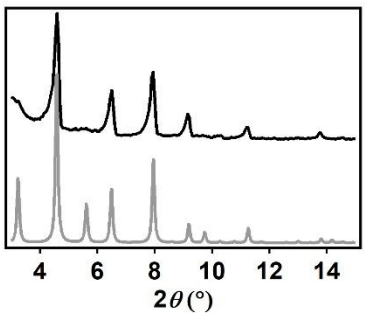

Figure 4. pXRD data of *d*PCN-224(Fe) synthesized in this work measured at 2°/min (black) and the theoretical diffractogram of PCN-224 (grey) that is based on the crystal structure of PCN-224 obtained by Zhou *et al*.[30]

The ORR activity of *d*PCN-224(Fe) is compared to the activity of FeTCPP to investigate the role of the porous environment of *d*PCN-224(Fe) on the ORR activity, selectivity, and stability of the catalyst under ORR conditions. Rotating disk electrode (RDE) measurements are carried out in which the glassy carbon working electrode is modified with a dropcast containing the catalyst, carbon black (CB) as an electron conducting additive, and Nafion as an adhesive binder to maintain the physical intactness of the layer. This ink was dropcasted onto a glassy carbon electrode and allowed to dry in air. The ORR activity was assessed with RDE cyclic voltammograms (RDE CVs) in an aqueous solution containing 0.15 M HNO_3 and 0.15 M $NaNO_3$ under an oxygen atmosphere.

It is important to note that other electrolytes were used as well, including acetate buffer (pH 4.7), phosphate buffer (pH 7), and borate buffer (pH 8.5) and non-buffered Na_2SO_4 (pH 5), $NaNO_3$ (pH 7), and NaOH (pH 14) electrolytes (SI 3). However, with all these electrolyte systems, the *d*PCN-224(Fe) MOF leached from the electrode during the first CV scan or directly when inserted into the electrolyte (Figure S2). The *d*PCN-224(Fe) dropcast only remained intact in acidic electrolytes of HNO_3, H_2SO_4 or $HClO_4$. Whereas other PCN-224(Fe) materials have been described to show good ORR activity in alkaline 0.1 M electrolyte solutions,[28] the cubic PCN-224(Fe) crystals obtained in this study are not stable in alkaline media and dissolve immediately.

RDE CV measurements of *d*PCN-224(Fe) and FeTCPP show that in the first scan both catalysts are active for the ORR resulting in large peak-shaped curves (Figure 5 and SI 4). The shapes of these curves are unusual for RDE experiments and indicate that an irreversible event is occurring during the ORR that is not mass transport limited in oxygen. Moreover, for *d*PCN-224(Fe) the current collapses upon the continuation of the CV experiment and after nine scans, the ORR activity is completely lost (Figure 5b). This behavior was also found for a sample of phase-pure PCN-224(Fe) in acidic aqueous electrolyte, which indicates that the absence of the long-range superstructure in *d*PCN-224(Fe) is not the cause of the decreasing ORR current (Figure S6). For FeTCPP, the change in the CV upon prolonged scanning is more gradual. The maximum current decreases while the catalytic wave shifts cathodically (Figure 5c). This RDE CV shows a plateau current with a cathodic peak at 0.25 V vs. RHE on top of the plateau. This additional cathodic peak might be indicative of a mismatch between the elementary steps during ORR catalysis.[45-47] If the first activation of the Fe superoxide intermediate via a proton and electron transfer is limiting catalysis, the Fe superoxide species might accumulate before it reacts toward the Fe hydroperoxo intermediate at a higher overpotential. If the activation of this Fe hydroperoxo species is limiting, H_2O_2 might form locally which is further reduced to H_2O at a higher potential.

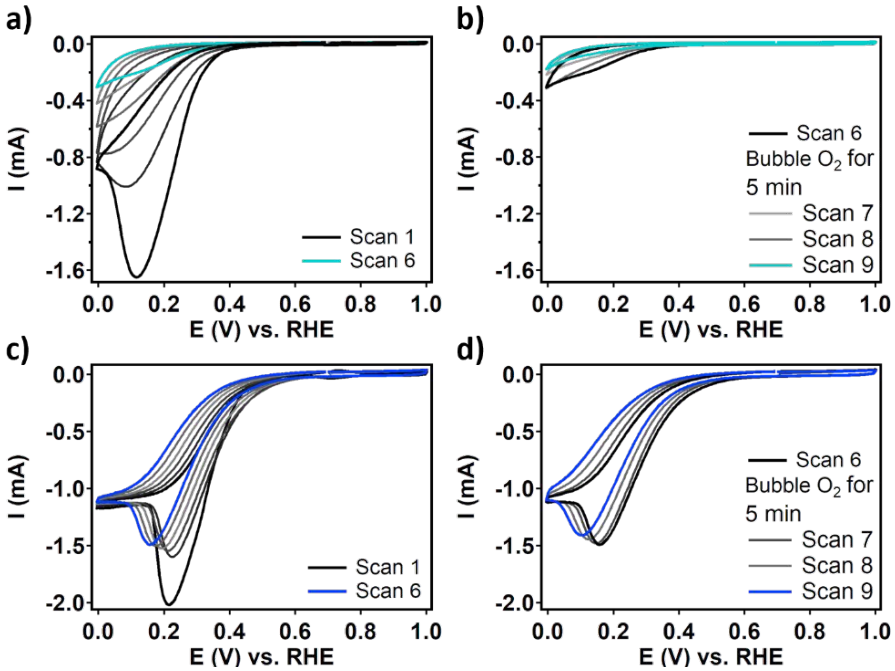

Figure 5. Six RDE CV scans of (a) *d*PCN-224(Fe) and (b) three RDE CV scans after bubbling oxygen for 5 minutes. Six RDE CV scans of (c) FeTCPP and (d) three RDE CV scans after bubbling oxygen for 5 minutes. Measured in 0.15 M HNO_3 and 0.15 M $NaNO_3$ with 50 mV/s scan rate and 1600 rpm rotation rate under an oxygen atmosphere.

View Article Online
DOI: 10.1039/D5SC01439C

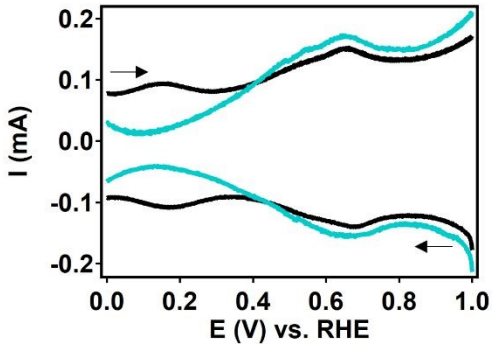

Figure 6. DPV measurement of dPCN-224(Fe) before (black) and after (teal) ORR electrocatalysis. Measured in 0.15 M HNO3 and 0.15 M NaNO3 with 2 mV step size, 50 mV modulation amplitude, 3 ms modulation time and 50 ms interval time under an argon atmosphere.

measuring DPV under argon atmosphere, the *d*PCN-224(Fe) sample was subjected to an RDE CV measurement of nine scans under oxygen atmosphere, after which DPV was recorded again under argon atmosphere (Figure 6). The DPV after electrocatalysis reveals that the redox couple at 0.17 V vs. RHE is no longer present.

From reports about photooxidation with *d*PCN-224(Fe) it is known that H_2O_2 and reactive oxygen species (ROS) can induce degradation of the catalyst.[33-37] To verify if H_2O_2 also plays a role in the irreversible diminishing of the ORR current for *d*PCN-224(Fe), the ORR selectivity is investigated. During the ORR, the two-electron oxygen reduction reaction (E^0 = 0.695 V vs. NHE) towards H_2O_2 is in competition with the four-electron oxygen reduction reaction towards H_2O (E^0 = 1.23 V vs. NHE). The faradaic efficiency of the ORR towards H_2O_2 (%H_2O_2) with *d*PCN-224(Fe) or FeTCPP is investigated with rotating rink disk electrode linear sweep voltammetry (RRDE LSV) experiments (SI

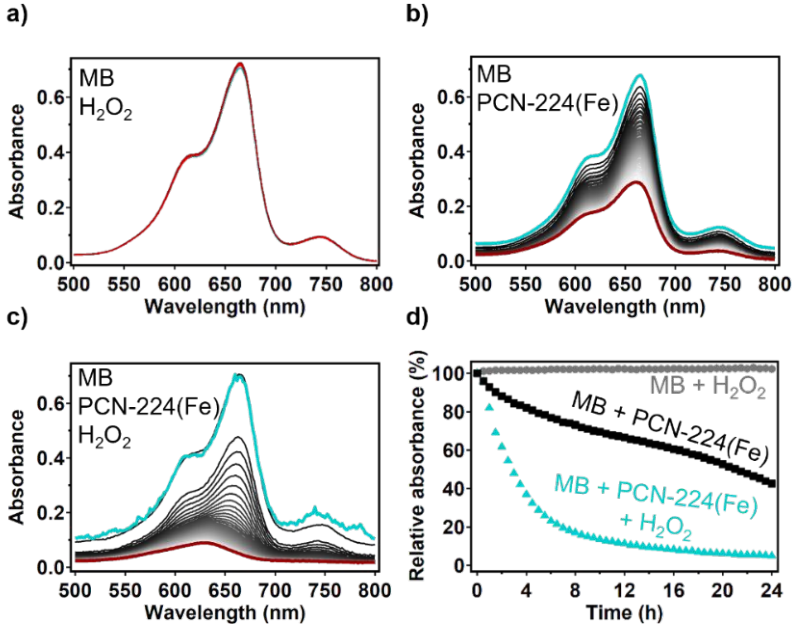

Figure 7. UV-Vis spectra with (a) MB and H_2O_2, (b) *d*PCN-224(Fe) and MB, and (c) *d*PCN-224(Fe), MB and H_2O_2 measured every 30 minutes for 24 h. The spectrum at t=0 is shown in teal and the curve at t = 24 h is shown in red. (d) The relative absorbance at 665 nm over time under the three different conditions: [MB+ H_2O_2] in grey, [*d*PCN-224(Fe)+MB] in black, and [*d*PCN-224(Fe)+MB +H_2O_2] in teal. Concentrations: 6.0 µg/mL MB, 10 mM H_2O_2, and 0.17 mg/mL PCN-224(Fe) with a total cuvette volume of 3 mL.

During the ORR, the iron species is reduced from Fe^{III} to Fe^{II} before oxygen binds (Figure 2). This redox couple can be visualized by measuring a differential pulse voltammetry (DPV) experiment in the absence of oxygen. Therefore, a DPV measurement was carried out under argon atmosphere with a fresh dropcast containing *d*PCN-224(Fe) (Figure 6). In the DPV trace two redox couples can be distinguished at 0.65 V vs. RHE and at 0.17 V vs. RHE. The peak at 0.65 V vs. RHE was also observed for PCN-224(H_2), which is the same MOF without the iron center coordinated in the porphyrin pocket (Figure S7). Broad peaks at around 0.6-0.7 V vs. NHE have previously been associated with proton-coupled electron transfers of quinone functionalities on a carbon support.[48, 49] Therefore, this peak is not expected to be related to the iron porphyrin complex. The peak at 0.17 V vs. RHE is assigned to the Fe^{II}/Fe^{III} couple.[50] After 7). To determine %H_2O_2 the average of three measurements was used. *d*PCN-224(Fe) shows a %H_2O_2 of ~19 ± 5% over the whole potential range, while FeTCPP shows a %H_2O_2 of ~ 32 ± 7% at 0.4 V vs. RHE and ~ 8 ± 2% at 0.15 V vs. RHE. These results

$$Fe^{3+} + H_2O_2 \longrightarrow Fe^{2+} + HO_2^{\bullet} + H^+ \quad (1)$$

$$Fe^{2+} + H_2O_2 \longrightarrow Fe^{3+} + HO^{\bullet} + OH^- \quad (2)$$

indicate that during the ORR with *d*PCN-224(Fe) and FeTCPP H_2O_2 is indeed being formed.

Reactive oxygen species (ROS) such as the hydroxyl radical can be formed by the Fenton reaction catalyzed by an iron species:[51] The possibility of an iron species to carry out the Fenton reaction depends on the nature of the iron species and the electrolyte.[52] An extensive study was carried out by Yang *et al.* in which the Fenton reaction catalyzed by FeTCPP was

View Article Online
DOI: 10.1039/D6SC01428C

investigated.[53] The FeTCPP catalyst was used to degrade the organic molecule bisphenol A in the pH range of 4 – 12. Via 5,5-dimethyl-1-pyrroline N-oxide (DMPO) trapping experiments, hydroxide radicals could be found in the reaction mixture. This indicates that the porphyrin site FeTCPP that is present in dPCN-224(Fe) is capable of Fenton chemistry. The ability of *d*PCN-224(Fe) to generate hydroxyl radicals from H_2O_2 was tested by combining the MOF with H_2O_2 and the organic dye methylene blue in 0.15 M HNO_3 and 0.15 M $NaNO_3$. Methylene blue (MB) is an organic dye that is specifically degraded by hydroxide radicals as shown by radical trapping experiments with DMPO in previous reports.[54-56] The degradation of the MB dye can be monitored with UV-Vis spectroscopy. The UV-Vis signal of MB was found to be stable after addition of H_2O_2 to the acidic MB solution (Figure 7a), which indicates that H_2O_2 itself cannot degrade MB. Combining the *d*PCN-224(Fe) MOF with the acidic MB solution resulted in 57% loss of MB signal after 24 h (Figure 7b). This loss of the UV-Vis signal of MB can be explained by absorption of the organic dye in the pores of the MOF, which was also observed with PCN-224(Co) (Figure S10) and the iron-based MOF NH_2-MIL-88B(Fe).[56] Upon addition of both the *d*PCN-224(Fe) and H_2O_2 to the acidic MB solution, a more rapid decrease of the MB signal is seen and 95% of the UV-Vis signal at 665 nm is lost after 24 h (Figure 7c-d). This large decrease of the UV-Vis signal of MB indicates that *d*PCN-224(Fe) can indeed generate hydroxyl radicals from H_2O_2 that degrade the MB dye. Moreover, upon addition of H_2O_2 to *d*PCN-224(Fe) the formation of bubbles was observed, which indicates that the MOF can also catalyse the disproportionation of H_2O_2 to water and oxygen (Figure S11). The activation of H_2O_2 by *d*PCN-224(Fe) is an interesting finding, since iron mostly has a Fe(III) oxidation state in this MOF, while it is Fe(II) that is expected to mostly accelerate Fenton chemistry via the reductive pathway. This leads to a slow activation of H_2O_2 in the UV-Vis experiment. During the electrochemical ORR, the iron sites are expected to be reduced to Fe(II) by the electrode material, which makes the iron sites more active for the Fenton reaction and fast decomposition of H_2O_2 to hydroxide radicals is expected.

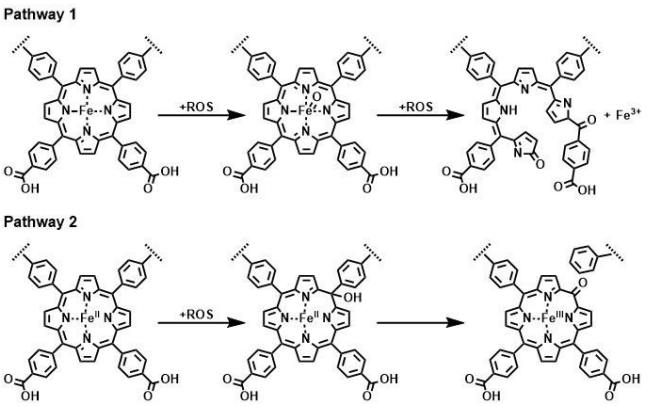

Figure 8. Reported degradation pathways of an iron porphyrin of the *d*PCN-224(Fe) MOF upon contact with a reactive oxygen species being either H_2O_2 or a radical species.[39, 57-59]

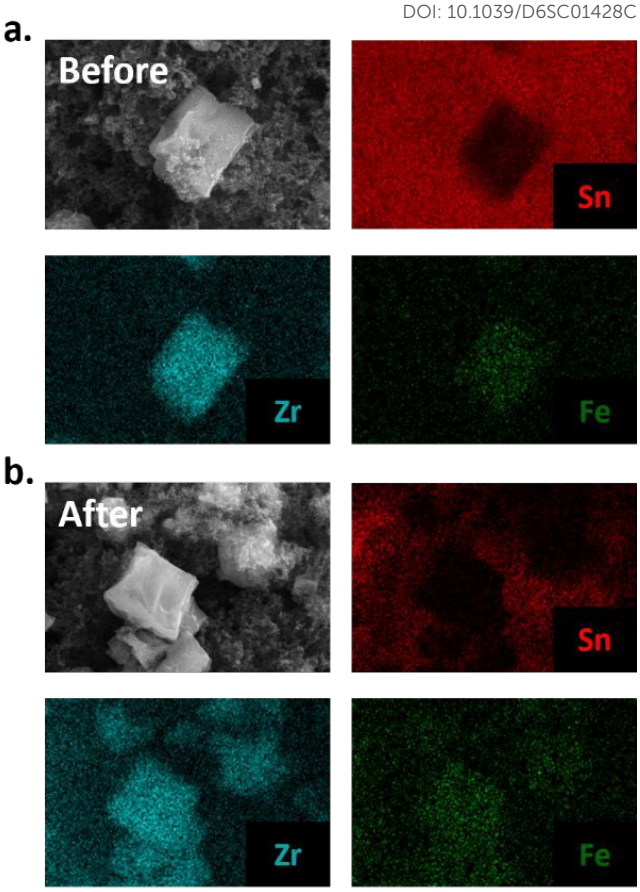

Figure 9. SEM-EDX of dPCN-224(Fe) (a) before and (b) after 20 CV cycles. Elemental mapping is given for Sn (red), Zr (teal) and Fe (green).

It was shown that *d*PCN-224(Fe) produces H_2O_2 during the electrochemical ORR and that *d*PCN-224(Fe) can degrade H_2O_2 into hydroxyl radicals. Therefore, the degradation of *d*PCN-224(Fe) might be caused by interactions of these radical species with the porphyrin linkers of the MOF. The interactions of ROS with iron porphyrins have been investigated previously.[58, 60-64] In nature, iron porphyrins of peroxidases are often damaged by the reaction of the heme with H_2O_2.[60] In this peroxidase, porphyrin degradation was found to proceed via ring-cleavage oxidation at the *meso*-position of the porphyrin. This porphyrin degradation mechanism via ring-opening with loss of iron ions was also found for *d*PCN-224(Fe) upon H_2O_2 treatment under UV-light irradiation (Figure 8).[39] Furthermore, degradation of an iron porphyrin in pyridine solution was found to occur due to attack by ROS and a degradation pathway in which the *meso*-position is oxidized with retention of the N_4-binding pocket of the porphyrin was identified (Figure 8).[57, 58] This pathway was also reported as possible degradation pathway of heme in nature, in which *meso*-hydroxyheme is formed upon interaction with hydrogen peroxide.[59] To understand what happens to *d*PCN-224(Fe) during the ORR, the structure and chemistry of *d*PCN-224(Fe) before and after catalysis was assessed with SEM, pXRD, inductively coupled plasma mass spectrometry (ICP-MS), X-ray photoelectron spectroscopy (XPS), solid state UV-Vis, and Fourier-transform infrared spectroscopy (FTIR) measurements.

View Article Online
DOI: 10.1039/D6SC01428C

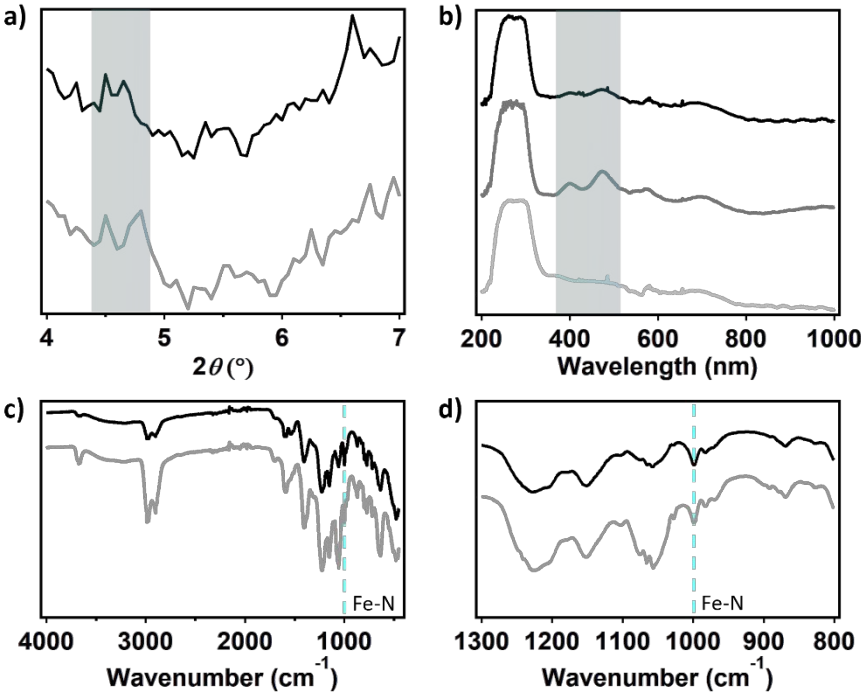

Figure 10. (a) pXRD before (grey) and after (black) catalysis of *d*PCN-224(Fe) ink on an FTO electrode. (b) UV-Vis of bare FTO (light grey), FTO with *d*PCN-224(Fe) fresh after dropcast (dark grey) and FTO with *d*PCN-224(Fe) after electrocatalysis (black). (c) FTIR of FTO with *d*PCN-224(Fe) fresh after dropcast (grey) and FTO with *d*PCN-224(Fe) after electrocatalysis (black) and (d) FTIR spectrum zoomed in between 1300 and 800 cm^{-1}.

To evaluate the morphology of the *d*PCN-224(Fe) particles before and after ORR catalysis, a fluorine doped tin oxide (FTO) electrode was covered with the catalyst ink solution and used for twenty CV cycles under oxygen atmosphere. During these 20 CV scans the activity was completely lost (Figure S12). After drying of the electrode, SEM images were collected of a fresh dropcast sample and a sample that was subjected to catalysis (Figure S13). The size and shape of the cubic particles are retained after catalysis. Moreover, elemental mapping with SEM-EDX (EDX = energy dispersive X-ray) measurements were carried out to identify the FTO background with Sn and the MOF particles with Zr and Fe contents (Figure 9). The elemental mapping indicates the presence of Zr and Fe at the position of the MOF particles before and after catalysis as well as Sn at the places without MOF particles. This indicates that the iron is not removed from the framework during catalysis. This was confirmed with ICP-MS analysis of *d*PCN-224(Fe) by dissolving a fresh dropcast of an FTO electrode and a dropcast of an FTO electrode used for catalysis in HNO_3 solution. In the fresh sample 2.09 ± 0.01 Fe ions per Zr_6 node were found, while the used samples showed 2.02 ± 0.10 Fe centers per node (SI 11). Moreover, XPS analysis of the dPCN-224(Fe) samples before and after catalysis illustrate that the MOF is retained during catalysis. Substantial amounts of Zr can be detected in samples before and after catalysis. However, Fe, due to its low surface concentration, could not be detected before and after catalysis. Also, the nitrogen content was too low to make a conclusive statement on the state of N from the N1s spectra. This may suggest that the outside of the MOF particles predominantly consist of Zr-nodes. pXRD measurements were carried out with the FTO electrode covered with the *d*PCN-224(Fe) ink to investigate the porosity of the framework after catalysis (Figure 10a). An FTO electrode was covered with 50 µL ink and used for 20 CV cycles under oxygen atmosphere (Figure S15). pXRD was measured of a fresh FTO electrode with *d*PCN-224(Fe) ink on it and of an FTO electrode used for electrocatalysis (Figure 10a). To obtain a dry sample after catalysis, the FTO plate with dropcast was soaked in water to remove electrolyte ions and in DCM to remove the water molecules and allow for drying. During these soaking cycles, some of the dropcast detached from the FTO electrode. Therefore, there are less MOF particles after catalysis than in a fresh dropcast, which leads to lower intensity signals in characterization methods used herein. Nevertheless, the pXRD indicates faint reflections at 4.6° for both FTO electrodes, which indicates the porosity is maintained after catalysis (Figure 10a).

Solid state UV-Vis was carried out to investigate the porphyrin UV-Vis absorbance of *d*PCN-224(Fe) before and after catalysis on an FTO electrode (Figure 10b). A *d*PCN-224(Fe) ink was made without CB, because the carbon would absorb all the light. The FTO electrode was used for 20 CV cycles under oxygen atmosphere (Figure S18). A bare FTO electrode, fresh dropcast on FTO and the dropcast used for electrocatalysis were investigated with solid state UV-Vis spectroscopy. The fresh dropcast shows two absorbance peaks at 399 and 473 nm that are not present for the bare FTO sample and originate from the porphyrin structure in *d*PCN-224(Fe). For FeTCPP a Soret band at 419 nm and a Q-band at 535 nm have been documented previously.[65, 66] Therefore, for *d*PCN-224(Fe) the absorption peaks are assigned to a Soret band at 399 nm and a Q-band at

473 nm, which is blue-shifted compared to FeTCPP itself. These absorption peaks are still present in the dropcast after catalysis, which indicates that the porphyrin structure remains intact.
FTIR was carried out with the same FTO electrodes without CB to investigate the bonds present in the *d*PCN-224(Fe) framework before and after electrocatalysis (Figure 10c). All peaks of the fresh sample are found back in the sample after catalysis and are assigned in Appendix D.9. Moreover, the vibration at 999 cm^{-1} of Fe-N is present in both spectra, which is indicative of the retention of Fe in the N_4-pocket of the porphyrin (Figure 10d).[35] Based on the SEM-EDX, ICP-MS, XPS, pXRD, solid-state UV-Vis, and FTIR measurements, it can be concluded that no significant change of the porphyrin and Zr node content has taken place after ORR catalysis with *d*PCN-224(Fe).

Discussion

For *d*PCN-224(Fe) the ORR activity is completely lost after nine consecutive CV cycles in oxygen environment. This is in contrast to the PCN-224(Co),[27] which is stable in presence of H_2O_2, thereby linking the observations in case of PCN-224(Fe) to the presence of iron. The analysis of the *d*PCN-224(Fe) structure before and after catalysis with SEM, pXRD, ICP-MS, solid state UV-Vis, and FTIR measurements were the same before and after catalysis, which entails that the bulk of the MOF remains unchanged after catalysis. This indicates that the complete shutdown of catalysis is not due to a complete destruction of the MOF particles. Interestingly, DPV measurements indicate the complete disappearance of the Fe^{II}/Fe^{III} couple after ORR catalysis, which indicates that there is no longer an electrochemical connection with Fe-sites in the MOF. The complete shutdown of catalysis, the disappearance of the Fe^{II}/Fe^{III} redox couple, and the retention of the bulk structure of the MOF points to key sites within the MOF framework to be decomposed. These sites could either have a role as a catalytic site or as an electron transfer site. Given that experiments with Fe-TCPP under the same conditions, and many other iron porphyrin systems reported in literature that do not rely on an electron transport chain,[67-70] do not breakdown in a spectacular manner under ORR conditions, irrespective of the presence of H_2O_2 and ROS generation, illustrates that the rapid breakdown of all catalytic activity in PCN-224(Fe) is an anomaly. The injection of the first electron from the electrode material to the MOF occurs at the Fe(III) sites that are closest to the electrode support. Electron conduction in MOFs with spatially separated electroactive linkers, such as *d*PCN-224(Fe), occurs via hopping between the porphyrin sites.[71-73] So upon reduction of this first critical Fe(III) site next to the electrode material to an Fe(II) species, the electron can be further transferred to an Fe(III) site in the vicinity. This electron hopping method then continues via a diffusion-like hopping mechanism through the framework.[23, 74] This electron hopping mechanism is thus dependent on the first electron transfer between the electrode material and the MOF particle. Upon this first electron transfer, the formed Fe(II) species next to the electrode interface can either continue with the electron hopping or bind oxygen to perform the ORR. During the ORR, H_2O_2 is formed which can react with Fe(II) to form ROS via the Fenton reaction and trigger decomposition.[74] When these critical sites of the framework near the electrode are damaged, the electron conduction pathway is impeded and catalysis will be completely halted (Figure 11), which would be in line with the severely more devastating collapse of catalytic activity in PCN-224(Fe) compared to Fe-TCPP and other Fe-porphyrin systems.

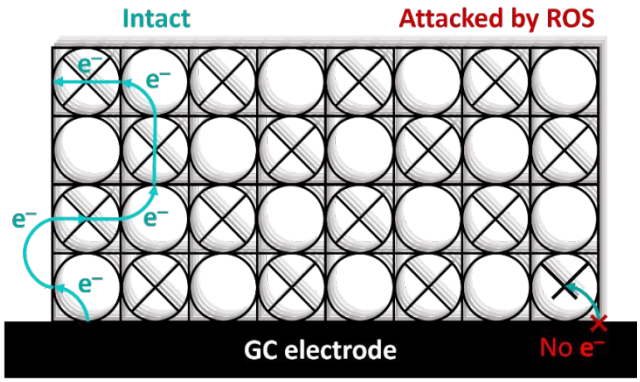

Figure 11. Schematic overview of electron conduction in dPCN-224(Fe) when intact or when the porphyrin site near the glassy carbon (GC) working electrode is inactive due to degradation.

Conclusions

From this work it can be concluded that changing the metal in the porphyrin pocket of the PCN-224 MOF from cobalt to iron can drastically change the stability, selectivity, and activity of the ORR electrocatalyst. Even though the majority of the PCN-224(Fe) MOF is perfectly intact, all electronic communication between the carbon support and the MOF is lost after a short burst of electrocatalysis.. This suggest, that even though the density of active sites is exceptionally high in MOF systems, the catalytic reaction is strongly dependent on the stability of only few active sites that are involved in the electron transfer chain. The dual role of the iron sites in electron transport and catalysis, and the stability issues associated, represent a major hurdle in the development of MOF systems as stable electrocatalysts.

Author contributions

DR: Investigation, writing original draft, writing – review & editing; RM: Investigation, writing original draft; ST: Resources; HK: Formal Analysis; JPH: Formal Analysis, Supervision, Resources; DGHH: Conceptualization, Funding Acquisition, Supervision, Writing – review & editing

Conflicts of interest

There are no conflicts to declare.

Data availability

The data supporting this article have been included as part of the supplementary information (SI). Supplementary information: N_2 isotherm, chemical stability *d*PCN-224(Fe), triplo RDE CV *d*PCN-224(Fe) and FeTCPP, RDE CV with PCN-224(Fe), DPV PCN-224(H_2), triplo RRDE LSV with *d*PCN-224(Fe) and FeTCPP, UV-Vis study with PCN-224(Co), bubble formation dPCN-224(Fe) and H_2O_2, SEM *d*PCN-224(Fe), ICP-MS *d*PCN-224(Fe), XPS *d*PCN-224(Fe), FTIR *d*PCN-224(Fe).

Acknowledgements

The authors acknowledge NWO for financial support (grant number 739.017.003). H. Kang acknowledges the Chinese Scholarship Council for financial support under fellowship no. 202206540004.

Notes and references

1. Y. T. Zheng, S. M. Li, N. Y. Huang, X. R. Li and Q. Xu, *Coord. Chem. Rev.*, 2024, **510**, 215858.
2. Q. J. Mo, C. Y. Chen, S. H. Li, J. W. Liu, L. Zhang and C. Y. Su, *ChemCatChem*, 2024, **16**, e202301753.
3. N. F. Suremann, B. D. McCarthy, W. Gschwind, A. Kumar, B. A. Johnson, L. Hammarström and S. Ott, *Chem. Rev.*, 2023, **123**, 6545-6611.
4. Y. Xin, Y. Cao, J. Yang, X. R. Guo, K. Shen and W. Yao, *J. Mater. Chem. A*, 2024, **12**, 4931-4970.
5. R. M. Zhu, L. M. Liu, G. X. Zhang, Y. Zhang, Y. X. Jiang and H. Pang, *Nano Energy*, 2024, **122**, 109333.
6. Z. Zhu, J. J. Duan and S. Chen, *Small*, 2024, **20**, 2309119.
7. Y. Peng, S. Sanati, A. Morsali and H. Garcia, *Angew. Chem. Int. Ed.*, 2023, **62**, e202214707.
8. R. Saha, K. Gupta and C. J. G. García, *Cryst. Growth Des.*, 2024, **24**, 2235-2265.
9. C. W. Kung, S. Goswami, I. Hod, T. C. Wang, J. X. Duan, O. K. Farha and J. T. Hupp, *Accounts of Chemical Research*, 2020, **53**, 1187-1195.
10. Z. H. Cheng, K. M. Fahy, G. W. Peterson, K. O. Kirlikovali and O. K. Farha, *Adv Mater*, 2025, **37**.
11. M. I. Severino, E. Gkaniatsou, F. Nouar, M. L. Pinto and C. Serre, *Faraday Discuss*, 2021, **231**, 326-341.
12. Y. An, X. L. Lv, W. Y. Jiang, L. L. Wang, Y. X. Shi, X. X. Hang and H. Pang, *Green Chem Eng*, 2024, **5**, 187-204.
13. C. H. Hsueh and C. W. Kung, *Acs Appl Mater Inter*, 2026, **18**, 4-18.
14. S. Yuan, J. Y. Peng, Y. R. Zhang and Y. Shao-Horn, *J Phys Chem C*, 2019, **123**, 28266-28274.
15. J. H. Cavka, S. Jakobsen, U. Olsbye, N. Guillou, C. Lamberti, S. Bordiga and K. P. Lillerud, *J Am Chem Soc*, 2008, **130**, 13850-13851.
16. S. Goswami, D. Ray, K. Otake, C. W. Kung, S. J. Garibay, T. Islamoglu, A. Atilgan, Y. X. Cui, C. J. Cramer, O. K. Farha and J. T. Hupp, *Chem Sci*, 2018, **9**, 4477-4482.
17. S. R. Mishra, V. Chavda, S. Roy, S. Rawat, S. Panda, N. Sarkar, S. K. K. Pasha, M. Ahmaruzzaman and B. M. Nagaraja, *Mater Today Nano*, 2025, **31**.
18. S. M. Pratik, L. Gagliardi and C. J. Cramer, *Chem Mater*, 2020, **32**, 6137-6149.
19. K. Hemmer, M. Cokoja and R. A. Fischer, *Chemcatchem*, 2021, **13**, 1683-1691.
20. J. Liu, T. A. Goetjen, Q. I. Wang, J. G. Knapp, M. C. Wasson, Y. Yang, Z. H. Syed, M. Delferro, J. M. Notestein, O. K. Farha and J. T. Hupp, *Chem Soc Rev*, 2022, **51**, 1045-1097.
21. F. K. Bi, J. F. Wei, B. Gao, S. T. Ma, N. Liu, J. C. Xu, B. L. Liu, Y. D. Huang and X. D. Zhang, *Environ Sci Technol*, 2024, **58**, 19797-19806.
22. M. E. Hoefnagel and D. G. H. Hetterscheid, *Chemsuschem*, 2025, **18**.
23. B. Johnson, A. M. Beiler, B. D. McCarthy and S. Ott, *J Am Chem Soc*, 2020, **142**, 11941-11956.
24. B. Johnson and S. Ott, *Chem. Sci.*, 2020, **11**, 7468-7478.
25. A. T. Castner, B. A. Johnson, S. M. Cohen and S. Ott, *J Am Chem Soc*, 2021, **143**, 7991-7999.
26. D. W. Feng, W. C. Chung, Z. W. Wei, Z. Y. Gu, H. L. Jiang, Y. P. Chen, D. J. Darensbourg and H. C. Zhou, *J Am Chem Soc*, 2013, **135**, 17105-17110.
27. D. Rademaker, S. Tanase, H. R. Kang, J. P. Hofmann and D. G. H. Hetterscheid, *Chem-Eur J*, 2024, **30**.
28. W. Yan, Q. L. Xing, O. Y. Guo, H. Feng, H. Y. Liu, P. Deshlahra, X. Y. Li and Y. L. Chen, *ACS Appl. Mater. Interfaces*, 2022, **14**, 50751–50761.
29. S. Sohrabi, S. Dehghanpour and M. Ghalkhani, *ChemCatChem*, 2016, **8**, 2356-2366.
30. M. L. Pegis, D. J. Martin, C. F. Wise, A. C. Brezny, S. I. Johnson, L. E. Johnson, N. Kumar, S. Raugei and J. M. Mayer, *J. Am. Chem. Soc.*, 2019, **141**, 8315-8326.
31. A. C. Brezny, S. I. Johnson, S. Raugei and J. M. Mayer, *J. Am. Chem. Soc.*, 2020, **142**, 4108-4113.
32. M. L. Rigsby, D. J. Wasylenko, M. L. Pegis and J. M. Mayer, *J. Am. Chem. Soc.*, 2015, **137**, 4296-4299.
33. C. H. Qi, S. P. Han, J. L. Lin, J. H. Cheng, K. S. Du, Y. Y. Hu and Y. C. Chen, *Catalysts*, 2022, **12**, 671.
34. L. Wang, P. X. Jin, S. H. Duan, J. W. Huang, H. D. She, Q. Z. Wang and T. C. An, *Environ. Sci. Nano*, 2019, **6**, 2652-2661.
35. L. Shi, L. Q. Yang, H. B. Zhang, K. Chang, G. X. Zhao, T. Kako and J. H. Ye, *Appl. Catal. B Environ.*, 2018, **224**, 60-68.
36. X. Lai, R. Y. Li, B. J. Zhang, T. T. Zhang, X. B. Ji, L. G. Wang, Y. S. Cui, H. Y. Xiao and D. X. Ning, *Colloid. Surface. Physicochem. Eng. Aspect.*, 2024, **680**, 132645.
37. C. C. Zhang, Y. K. Yan, H. B. Huang, X. S. Peng, H. Song, J. H. Ye and L. Shi, *ACS Catal.*, 2023, **13**, 15351-15359.
38. Y. Q. Zong, S. S. Ma, J. M. Gao, M. J. Xu, J. J. Xue and M. X. Wang, *ACS Omega*, 2021, **6**, 17228-17238.
39. Y. F. Shu, X. Liu, M. Zhang, B. Liu and Z. Y. Wang, *Appl. Catal. B Environ. Energy*, 2024, **346**, 123749.
40. S. Sinha, M. S. Aaron, J. Blagojevic and J. J. Warren, *Chem. - Eur. J.*, 2015, **21**, 18072-18075.
41. D. W. Feng, Z. Y. Gu, J. R. Li, H. L. Jiang, Z. W. Wei and H. C. Zhou, *Angew. Chem. Int. Ed.*, 2012, **51**, 10307-10310.
42. D. Rademaker, S. Tanase, H. R. Kang, J. P. Hofmann and D. G. H. Hetterscheid, *Chem. -Eur. J.*, 2024, **30**, e202401339.
43. H. L. B. Bostrom, S. Emmerling, F. Heck, C. Koschnick, A. J. Jones, M. J. Cliffe, R. Al Natour, M. Bonneau, V. Guillerm, O. Shekhah, M. Eddaoudi, J. Lopez-Cabrelles, S. Furukawa, M. Romero-Angel, C. Marti-Gastaldo, M. Yan, A. J. Morris, I. Romero-Muniz, Y. Xiong, A. E. Platero-Prats, J. Roth, W. L. Queen, K. S. Mertin, D. E. Schier, N. R. Champness, H. H. Yeung and B. V. Lotsch, *Adv. Mater.*, 2023, **36**, e2304832.
44. C. Koschnick, R. Staglich, T. Scholz, M. W. Terban, A. von Mankowski, G. Savasci, F. Binder, A. Schokel, M. Etter, J. Nuss, R. Siegel, L. S. Germann, C. Ochsenfeld, R. E.

Dinnebier, J. Senker and B. V. Lotsch, *Nat. Commun.*, 2021, **12**, 3099.
45. N. Talukder, Y. D. Wang, B. B. Nunna and E. S. Lee, *Catalysts*, 2022, **12**, 791.
46. S. Shin, Y. Yoon, S. Park and M. W. Shin, *J. Alloys Compd.*, 2023, **939**, 168731.
47. A. C. Brezny, H. S. Nedzbala and J. M. Mayer, *Chem. Commun.*, 2021, **57**, 1202-1205.
48. C. J. Kaminsky, S. Weng, J. Wright and Y. Surendranath, *Nat. Catal.*, 2022, **5**, 430-442.
49. M. G. Sullivan, B. Schnyder, M. Bärtsch, D. Alliata, C. Barbero, R. Imhof and R. Kötz, *J. Electrochem. Soc.*, 2000, **147**, 2636-2643.
50. C. T. Carver, B. D. Matson and J. M. Mayer, *J. Am. Chem. Soc.*, 2012, **134**, 5444-5447.
51. J. Y. Xiao, S. F. Guo, D. Wang and Q. An, *Chem. - Eur. J.*, 2024, **30**, e202304337.
52. G. Bae, M. W. Chung, S. G. Ji, F. Jaouen and C. H. Choi, *ACS Catal.*, 2020, **10**, 8485-8495.
53. X. R. Yang, J. P. Hu, L. S. Wu, H. J. Hou, S. Liang and J. K. Yang, *Environ. Pollut.*, 2022, **313**, 120097.
54. S. Iwamori, N. Nishiyama and K. Oya, *Polym. Degrad. Stab.*, 2016, **123**, 131-136.
55. X. L. Teng, J. F. Li, Z. Y. Wang, Z. Wei, C. Z. Chen, K. Q. Du, C. Zhao, G. Yang and Y. Li, *RSC Adv.*, 2020, **10**, 24712-24720.
56. J. C. He, Y. Zhang, X. D. Zhang and Y. M. Huang, *Sci. Rep.*, 2018, **8**, 5159.
57. H. Kalish, J. E. Camp, M. Stepien, L. Latos-Grazynski and A. L. Balch, *J. Am. Chem. Soc.*, 2001, **123**, 11719-11727.
58. H. Schulenburg, S. Stankov, V. Schünemann, J. Radnik, I. Dorbandt, S. Fiechter, P. Bogdanoff and H. Tributsch, *J. Phys. Chem. B*, 2003, **107**, 9034-9041.
59. L. Avila, H. W. Huang, C. O. Damaso, S. Lu, P. Moënne-Loccoz and M. Rivera, *J. Am. Chem. Soc.*, 2003, **125**, 4103-4110.
60. B. Valderrama, M. Ayala and R. Vazquez-Duhalt, *Chem. Biol.*, 2002, **9**, 555-565.
61. D. Banham, S. Ye, K. Pei, J. Ozaki, T. Kishimoto and Y. Imashiro, *J. Power Sources*, 2015, **285**, 334-348.
62. L. Y. Wan, K. M. Zhao, Y. C. Wang, N. A. Wei, P. Y. Zhang, J. Y. Yuan, Z. Y. Zhou and S. G. Sun, *ACS Catal.*, 2022, **12**, 11097-11107.
63. S. Baranton, C. Coutanceau, C. Roux, F. Hahn and J. M. Léger, *J. Electroanal. Chem.*, 2005, **577**, 223-234.
64. N. A. Stephenson and A. T. Bell, *J. Am. Chem. Soc.*, 2005, **127**, 8635-8643.
65. B. H. Yao, C. Peng, W. Zhang, Q. K. Zhang, J. F. Niu and J. E. Zhao, *Appl. Catal. B Environ.*, 2015, **174**, 77-84.
66. B. H. Yao, C. Peng, Y. Q. He, W. Zhang, Q. K. Zhang and T. Zhang, *Catal. Lett.*, 2016, **146**, 2543-2554.
67. S. Rathi, I. Ahmad and M. Sankar, *Chem Commun*, 2025, **61**, 8512-8515.
68. C. Costentin, H. Dridi and J. M. Savéant, *J Am Chem Soc*, 2015, **137**, 13535-13544.
69. L. S. Xie, X. P. Zhang, B. Zhao, P. Li, J. Qi, X. N. Guo, B. Wang, H. T. Lei, W. Zhang, U. P. Apfel and R. Cao, *Angew Chem Int Edit*, 2021, **60**, 7576-7581.
70. Q. Hua, K. E. Madsen, A. M. Esposito, X. Y. Chen, T. J. Woods, R. T. Haasch, S. T. Xiang, A. Frenkel, T. T. Fister and A. A. Gewirth, *Acs Catal*, 2022, **12**, 1139-1149.
71. I. Hod, M. D. Sampson, P. Deria, C. P. Kubiak, O. K. Farha and J. T. Hupp, *ACS Catal.*, 2015, **5**, 6302-6309.
72. P. M. Usov, S. R. Ahrenholtz, W. A. Maza, B. Stratakes, C. C. Epley, M. C. Kessinger, J. Zhu and A. J. Morris, *J. Mater. Chem. A*, 2016, **4**, 16818-16823.
73. P. M. Usov, B. Huffman, C. C. Epley, M. C. Kessinger, J. Zhu, W. A. Maza and A. J. Morris, *ACS Appl. Mater. Interfaces*, 2017, **9**, 33539-33543.
74. A. T. Castner, H. Su, E. S. Grape, A. K. Inge, B. Johnson, M. S. G. Ahlquist and S. Ott, *J Am Chem Soc*, 2022, **144**, 5910-5920.
75. S. Y. Lin, P. M. Usov and A. J. Morris, *Chem. Commun.*, 2018, **54**, 6965-6974.

View Article Online
DOI: 10.1039/D6SC01428C

The datasets supporting this article have been uploaded as part of the supplementary information